Charge carrier transport dynamics in W/Mo-doped BiVO4 : first principles-based mesoscale characterization

Journal:	*Journal of Materials Chemistry A*
Manuscript ID	TA-ART-10-2018-009899.R1
Article Type:	Paper
Date Submitted by the Author:	20-Nov-2018
Complete List of Authors:	Pasumarthi, Viswanath; University at Buffalo, The State University of New York, Chemical and Biological Engineering Liu, Taifeng; Henan University, National & Local Joint Engineering Research Center for Applied Technology of Hybrid Nanomaterials, Collaborative Innovation Center of Nano Functional Materials and Applications of Henan Province Dupuis, Michel; University at Buffalo, State University of New York, Department of Chemical and biological engineering and Computation and Data-enabled Science and Engineering Program Li, Can; Dalian Institute of Chemical Physics, State Key Laboratory of Catalysis;

Charge carrier transport dynamics in W/Mo-doped $BiVO_4$: first principles-based mesoscale characterization.

Viswanath Pasumarthi[1], Taifeng Liu*[2], Michel Dupuis*[1,3,4], and Can Li[4,5]

1. Department of Chemical and Biological Engineering, University at Buffalo, Buffalo NY, USA
2. National & Local Joint Engineering Research Center for Applied Technology of Hybrid Nanomaterials, Collaborative Innovation Center of Nano Functional Materials and Applications, Henan University, Kaifeng, 475004, China
3. Computational and Data-Enabled Science and Engineering Program, University at Buffalo, Buffalo, NY, USA
4. Dalian National Laboratory for Clean Energy, Dalian Institute of Chemical Physics, Dalian, China
5. State Key Laboratory of Catalysis, Dalian Institute of Chemical Physics, Dalian, China

Abstract

We present a mesoscale characterization of carrier transport in W/Mo-doped ms-$BiVO_4$ (BVO) to supplement our earlier study of electron and hole transport in bulk BVO. The mesoscale kinetic Monte Carlo (KMC) approach, informed by first principles-determined electron and hole hopping rates, captures the complex dynamics of electron carriers arising from light absorption and from metal doping. The computations and simulations support the observation that, for the doping level used in experiment, doping atoms do not affect significantly the transport dynamics proper of the charge carriers compared to stoichiometric BVO. W/Mo doping increases the electron carrier concentration, and consequently the electrode conductivity. We used a density functional theory DFT+U method to characterize the electronic structure of doped BVO. Each W and Mo atom brings one more valence electron than a V atom. These excess electrons are mobile. We adopted the theories and methods of our earlier investigations on BVO. The DFT+U theory affords an accurate description of small electron polarons with electron localized on either W or Mo or V, as well as of the hopping barriers from W/Mo-to-V or V-to-V. Calculations on a 3x3x1 supercell of W/Mo-doped ms-BVO indicate that the excess electron from W or Mo does not reside on the doping atom. There is a shallow interaction region around the doping atom where the excess electron localized on a V atom is more stable than when localized on the doping atom, and slightly more stable than when the excess electron is localized far away from the doping atom. This region is two nearest V atom-wide for W and three nearest atom-wide for Mo. The depths of these stabilization regions are very small, ~ - 0.65 k_BT (at 300°K) for W and ~ - 0.73 k_BT for Mo. Calculated V-to-V hopping barriers in doped material are little affected within the region and not affected outside the region. Using our recently developed lattice-based kinetic Monte Carlo code adapted to account for doping atoms and their energy stabilization regions, we calculated the diffusivity of electrons for carrier density relevant to experiment, as well as the conductivity. The stabilization regions have little effect on the diffusivity compared to the stoichiometric system because of the smallness of the stabilization. The diffusivity is found to decrease slightly with an increasing number of carriers, but the conductivity of a system with electron polarons arising from doping together with light absorption increases compared to the un-doped system. This work will set the foundation to study electron transport in gradient (W/Mo)-doped systems and other mixed phase systems.

I. Introduction

The holy-grail in efficient and cost-effective conversion of solar energy into electrical and chemical energy is solar energy-driven water splitting using semi-conductor-based photo-catalysts. Photoelectrochemical (PEC) cells are attractive due to their design whereby the direct contact between semiconductor and liquid electrolyte integrates efficiently the processes of light absorption and conversion of generated charge carriers. Such a design is much simpler and potentially more efficient than 'integrated photovoltaic-electrolysis cells'. [1, 2] In any system intended for harvesting solar energy, including PEC cells, the semiconductor material plays the most crucial role. Semiconductor electrodes absorb the sunlight and create excited charge carriers (electrons and holes). Upon separation, these charge carriers generate an electronic potential that, if suitable, can drive the electrochemical reaction(s) at the surface of the electrode. Thus, the choice of semiconductor material is critical in governing the performance of PEC cells. The characteristics of an viable photo-electrode are: (i) it must generate a sufficient voltage to split water; (ii) it must have a suitable bandgap to harvest a significant portion of the solar spectrum while developing a sufficient photo-potential to drive the water splitting reactions; (iii) it must have band edges well-positioned to support the water splitting half-reactions; (iv) it must exhibit long-term stability in aqueous and oxidizing conditions; (v) it must require minimal kinetic over-potentials for charge transfer processes at the semiconductor–liquid junction (SCLJ); and, lastly, (vi) the semiconductor material must be made of abundant and cheap chemical elements. [1-3]

In the pursuit of ideal materials, semiconducting transition metal oxides are considered as potential candidates primarily owing to their chemical stability in aqueous environments. However, poor semiconducting properties of binary oxides have resulted so far in small photocurrents compared to theoretical maxima. [1] The limited efficiency in extracting the photo-generated charge carriers prompted a shift towards ternary and more complex multinary oxides. Among the large number of possible combinations for mixed metal oxides [4], bismuth vanadate $BiVO_4$ (BVO) is one of the highest performing ternary metal oxide photo-anode material reported to date. [1] The most active polymorph of BVO has the monoclinic-scheelite crystal structure (ms-BVO) with impressive theoretical efficiency limits of photocurrent densities. [5] The excellent activity of ms-BVO is a result of its well suited band structure for water splitting with an indirect band gap of ~2.4-2.5 eV [6] and a favorable conduction band edge positioned close to thermodynamic hydrogen evolution reaction (HER) potential. [7] However, the major limitations that hinders this material towards achieving theoretical efficiencies are rather poor electron-hole separation [7], poor electron transport [8], and poor water oxidation kinetics. [9] In order to address these challenges, a wide variety of strategies have been implemented, which include morphology control, doping, and, finally, coupling with oxygen evolution catalysts. [9]

Of the above mentioned strategies, doping BVO with either Mo^{6+} [10, 11] or W^{6+} [12, 13] or simultaneous doping with Mo^{6+} and W^{6+} [8] at the V^{5+} sites [14] was found to be effective in increasing photo-electro-catalytic activity in terms of electronic conductivity. A general observation resulting from these doping studies is an increased carrier density as interpreted from Mott-Schottky plots. [15] A consequence of the influx of excess mobile electrons from dopant sites resulting in an increased carrier density $\boldsymbol{n}$ and thus an increase in electrical conductivity $\boldsymbol{\sigma}$ according to:

$$\sigma = ne\mu \tag{1}$$

where $\boldsymbol{e}$ is the elementary charge, and $\boldsymbol{\mu}$ is the carrier mobility.

Carrier transport in BVO and (W/Mo)-doped BVO has been the subject of many recent experimental and computational investigations, including from our group. [16] [17] [18] [19] [20] [21] [22] [23] We recently reported first principles-based mesoscale simulations of electron and hole transport in stoichiometric bulk BVO [16], whereby hopping activation energies were obtained from DFT+U calculations. This earlier work is illustrated in Figure 1. We determined all possible hopping energies for electrons and for holes. We reported selected cluster calculations of the electronic coupling (V_{AB}) underlying the small polaron theory that led us to identify the strong non-adiabatic character of the electron transport processes. We assigned values of $\Delta G^* \sim 0.37$ eV for electron hops corresponding to a reorganization energy (in Marcus parlance) $\lambda \sim 1.48$ eV. Hole transport was shown to be bimodal, with fast but not transport-efficient hops among pairs of VO_4 tetrahedra and slow but transport efficient hops across VO_4 pairs. Nonetheless, electron mobility is about one order of magnitude smaller than hole mobility, so that conductivity in BVO is gated by electron transport. We determined that electron hops have V_{AB} electronic coupling (in Marcus/Holstein parlance) values of ~ 600 cm^{-1}, confirmed by

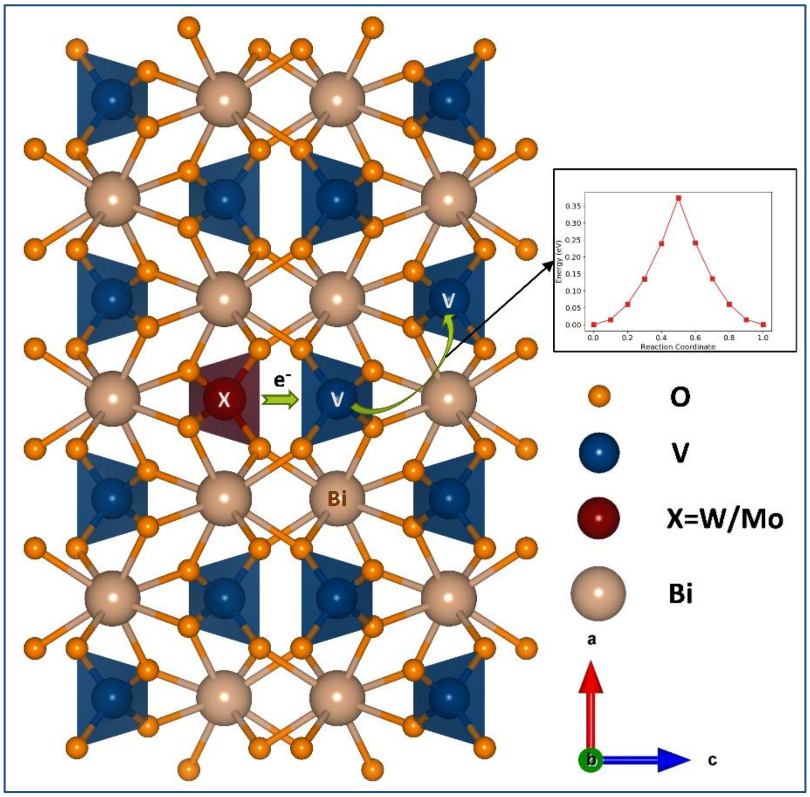

Figure 1 Crystalline structure of ms-BVO comprising 4 chemical structures per unit cell. MO_4 (M=V/W/Mo) units are shown in polyhedra. Figure illustrates the migration of excess electron from dopant site (X=W/Mo) to a neighboring V site. A typical energy profile of electron hopping (through-space) between two V sites is illustrated in the inset. The intersecting of potential energy curves were determined along the pathway interpolated between the initial and final participating polaron structures with their localized wavefunction states.

Constraint DFT calculations[22], in-between the regimes of diabatic and adiabatic hopping. Our value of ΔG^* for electron polarons is in good accord with the drift mobility experimental value of $\Delta G^* \sim 0.300$ eV.[24] Lattice-based KMC showed that both electron and hole mobility decrease slightly with increasing carrier density.

Abdi et al. [20] and Han et al. [21] showed that gradient doping of BVO by W atoms into n^+-n homojunctions was a successful strategy in increasing carrier separation and BVO's overall conversion efficiency. Jovic *et al.* [18] [19] used soft X-ray absorption spectroscopy to establish key characteristics of W/Mo-doping in ms-BVO: the excess electron from W/Mo does not reside on the doping atom, but rather as a small polaron localized on V sites. They also observed a small anisotropy in electronic structure between the *ab*-plane and the *c*-axis. Our earlier study [16] yielded also such a finding at the level of the dynamics. Overall, these authors concluded that the "improved conversion efficiency of W-doped BVO relative to the un-doped material is largely due to the increased carrier concentration in spite of increased carrier recombination rates".

Park et al. [8] applied DFT+U approach to understand the effects of W or Mo doping on the electronic structure of BVO. They found that the excess electron from W or Mo localizes on V atoms and creates a localized state in the band gap. The small polaron formation involves a sizable lattice distortion around the reduced V^{4+} ion. They suggested that the excess electron residing at the V^{4+} site may undergo migration to an adjacent V^{5+} (or Mo^{6+}, W^{6+}) site. Yin et al. [25] studied the extrinsic doping properties of BVO and they found substitutional Mo and W atoms on V sites are very shallow donors and have very low formation energies. Ding et al. [26] explored the origin of the enhanced photocatalytic activity of Mo-doped BVO using DFT. They showed that the Mo atoms prefer to substitute the V atoms in the bulk phase, but that for the (010) surface, Mo atoms prefer to substitute Bi atoms at the outermost layer. Overall it is accepted that doping of Mo or W in BVO bring excess electrons and these electron form mobile small polarons.

Wu et al. [22] and Zhang et al. [23] provided further experimental evidence and computational understanding why W-doping and Mo-doping is at the source of higher photocurrent. Several DFT-based levels of theory showed that the excess electron from W and Mo does not like the doping site but becomes a small polaron in the material. They calculated a hopping activation energy of $\Delta G^* \sim 0.25$ eV and suggested that hopping barriers are reduced by the presence of doping atoms due to some strong electrostatic interactions. This value is somewhat smaller than our previously reported value of ~ 0.37 eV [16] and also smaller than the experimental value of ~ 0.30 eV.

In this paper, we report on the nature of the stability and mobility of electron polarons in ms-BVO when doped with W or Mo as substitutions at V sites. QM calculations confirm that the excess electron localization on W/Mo sites is energetically unfavorable. At the same time, localization of the excess electron becomes energetically favorable by a small amount on V sites extending up to ~ the 3rd nearest neighbor shell in the vicinity of the dopant site. It is widely accepted that slow carrier transport in complex metal oxides arises from the nature of carrier localization in the form of small polarons [3, 27], so that the characterization of the electron transport in doped systems ought to account for the stabilization (trapping) near the dopant sites.

Using data from first-principle calculations, we performed KMC simulations to characterize the nature of electron transport in the presence of extrinsic doping in ms-BVO. The paper is organized as follows: in Section II we describe the computational methods and details, first about the DFT calculations, then about the KMC implementation, in particular with regards to the treatment of substitutional defects. In Section III we present and discuss the results. We conclude in Section IV.

II. Computational methods

a. DFT calculations:

We performed spin-polarized DFT calculations using the Vienna ab initio Simulation Package (VASP).[28, 29] The exchange correlation potential was described by the Perdew-Burke-Ernzerhof (PBE) functional within the generalized gradient approximation. [30] The projector augmented wave method was applied to describe electron-ion interactions.[31, 32] We used the +U correction approach for the self-interaction correction [33], using the values of $+U_{eff} = (U - J) = 5.0$ eV ($J = 1.0$ eV) on V(3d), W(5d), Mo(4d) states when performing charge localization calculations. The $+U_{eff}$ value on d orbitals of metal ions are taken from earlier work[16], affording localization of electron polarons on desired sites. The +U values on Mo(4d) and W(5d) were taken as the same as for V(3d). We used a 3x3x1 supercell with 216 atoms. A plane-wave cutoff energy of 400 eV and a (1x1x2) k-point mesh were used for geometry optimization. The Γ-centered k-point mesh of the Brillouin zone sampling was set at (2x2x1) based on the Monkhorst–Pack scheme.[34] The structures were relaxed until all forces on ions were less than 0.01 eV $Å^{-1}$. The core electrons were represented with pseudo-potentials with 6, 11, 12, 12, and 5 valence electrons for plane-wave description of O, V, W, Mo and Bi respectively. We used the conjugate gradient algorithm for ionic convergence with an energy difference cutoff set to 1.0E-05 eV. For Mo or W single doping, one V atom was substituted by one Mo or W atom in the supercell corresponding to a concentration of ~ 2.8 %. As for Mo and W co-doping, two V atoms far away from each other are substituted by Mo and W atom in the supercell.

b. Polaron modeling:

To describe polaron hopping, we made use of the Marcus/Holstein two-state model, of which several descriptions exist.[35-40] The details of how to use DFT to obtain the important parameters of Marcus theory are published in several of these papers [36-38, 41], including the definition of approximate reaction pathways. These papers describe also how to use the DFT data to get diffusion and mobility from Einstein's model of diffusion. In brief, the 'initial' and 'final' states in the two-state model of polaron hop correspond to localized spin densities on the 'initial' or 'final' sites respectively, with the structures being optimized to give the lowest energy structure of the 'localized' polaron states. The spin density arises from one excess electron for electron hops and the removal of one electron from the supercell for hole hops. The approximate reaction pathway is generated by morphing linearly the 'initial' polaron stable structure and the 'final' polaron structure. DFT energies are calculated for several points along the pathway, possibly using the previous electron density as initial guess of the DFT calculation to facilitate maintaining the localized spin character which we monitored. Such energy curves correspond to the 'quasi-diabatic' energy states when the localized spin character is maintained along the pathway, and most importantly at mid-point (crossing point). When the unpaired spin is shared by the 'initial' and 'final' sites at mid-point, the curves correspond to the 'adiabatic' energy states. Calculated polaron curves for doped systems are shown in the Supplementary Information.

In our earlier work[16], we stated and showed that the electronic coupling elements $\boldsymbol{V_{AB}}$ for all electron hops in bulk un-doped BVO are small, consistent with the cuspy Marcus curves and their non-adiabatic character. We adopted the same approximation for electron hops in doped BVO. Dopant atoms were found to be essentially inaccessible as electron localization sites, with the free energy increases for electron localization on W/Mo sites being ~ 26.12 k_BT and ~ 3.15 k_BT respectively relative to their first shell V sites, so that hops to W/Mo sites could be taken out the list of KMC processes (for W) or treated with negligible $\boldsymbol{V_{AB}}$ coupling (for Mo).

We note that for organic semiconductors (like pentacene and other), dynamic disorders arising from thermal effects have been shown to lead to large fluctuations in structures and consequently in electronic coupling and that carrier transport can be significantly affected by such fluctuations in some cases.[42] Unlike in these cases where the molecules in organic crystals are held together by weak interactions, bonding in inorganic crystals like BVO is much stronger and structural deformations due to temperature effects are expected to be much less significant than in organic crystals. It transpired also from our earlier work [16] that the reorganization energy (in Marcus/Holstein parlance) is large (λ ~ 1.48 eV based on ΔG^* ~ 0.37 eV). The magnitude of the electronic coupling $\boldsymbol{V_{AB}}$ (~ 600 cm^{-1} or less) is thus much smaller than the reorganization energy, and thermally-induced fluctuations of $\boldsymbol{V_{AB}}$ are unlikely to have a significant qualitative effect on predicted diffusivity and conductivity, in support of the applicability of the Marcus/Holstein small polaron hopping formalism.

c. KMC modeling:

For an ensemble of polarons, each of which may undergo a number of hops, it is necessary to solve the coupled kinetics to describe the transport. To this end we implemented a lattice-based Kinetic Monte Carlo simulation code.[43-45] Lattice-based KMC is an approach that is particularly well suited to describing the dynamics of space-charge distribution in complex systems such as those considered here. In brief KMC involves creating a list of processes (eight possible nearest-neighbor hops for each electron polaron), each process having its own rate (Eq. (2)). KMC uses a

$$k_{et} = n v_n \exp\left(-\frac{\Delta G^*}{k_B T}\right) \tag{2}$$

stochastic algorithm to solve the coupled rate equations, leading to a spatial and temporal characterization of the charge carrier distribution. Starting from a random distribution of a set of electron polarons across vanadium sites, the electrons 'move' stochastically in the presence of the other electrons during a simulation. The rate constants used at the start of the KMC simulations are taken from the DFT calculations described above. At each time step, the spatial distribution of the electrons affects differentially the vanadium site potentials, the polaron energies, and therefore the hopping rates. The site potentials are calculated through a Ewald summation approach because of the long-range nature of electrostatic interactions. The change in site relative energy for a polaron hopping from an 'initial' site to a 'final' site affects the activation energy for that hop, in accord with Marcus' expression in Eq. (3) or the Bell-Evans-Polanyi principle [46, 47], and, as a

$$\Delta G^{*} = \frac{(\lambda + \Delta G^{0})^{2}}{4\lambda} - V_{AB} \tag{3}$$

consequence, its associated rate. As the space-charge distribution evolves, so do all the individual hopping rates. A detailed description of the program can be found in the Appendix. For a given concentration of charge carriers, the initial spatial distribution of the carriers and of the dopant sites is randomly generated. The diffusivity is calculated from the average of the mean square displacements (MSD) of each electron (or hole), evaluated for 100 trajectories of 10 milliseconds each.

Special considerations are in order for doped systems. For un-doped ms-BVO, atoms are used as lattice sites carrying a charge equal to the full oxidation state of the constituent elements (Bi, V, O have oxidation states +5, +3, and -2 respectively). When a dopant W/Mo is introduced as a substitution for a V atom, we learn from the QM calculations (see below) that the W/Mo substitution creates a region of small stabilization for electron localization right around the site of substitution, extending up to ~ 3 nearest neighbor shells. In other words, the sites belonging to 4th and higher nearest neighbor shells are treated as unaffected and belonging to the 'bulk' region, vis-à-vis the substitution site. At the same time, electron localization at the W/Mo site of substitution is made virtually impossible as observed in earlier studies.[18, 19, 22] Accordingly the 'coordination' states of the W or Mo atoms are +5, with each dopant atom giving away an itinerant excess electron to the lattice. This observation made it possible to incorporate into the KMC model the effect of substitutions by W/Mo atoms by simply keeping the lattice site charges as +5 at the dopant sites, while adding one excess electron to the system. In this fashion the energy of any polaron distribution (calculated by Ewald summation) would remain unchanged if it were not for electron polarons being localized on V sites inside the region of interaction of the dopant atom. The interaction region was then modeled by adding a (small) stabilization energy contribution to V sites inside the region. This is the quantity ΔG_0 in Marcus/Holstein expression of Eq. (3). The modified activation energy ΔG^* is given by Eq. (3) and the altered rate is given by Eq. (2). The magnitude of the stabilization energy was derived from DFT calculations for W/Mo doped supercells. For W dopants the W site was found to be very high in energy and the site was removed as a c site to which electron polarons might hop to (in the list of possible KMC processes). For Mo dopants, the Mo site was given a relative energy of ~ + 0.012 eV, giving it a ~ 5 % probability of holding an excess electron (see results below). All in all, doping was captured in the KMC model without modifying the electrostatics of the system lattice in terms of lattice site charges.

In this paper we studied the electron transport characteristics (mobility and conductivity) over a range of doping levels. Each data point in the figures represents the average quantity over 100 trajectories, with each trajectory initialized from a unique spatial distribution of dopant sites in the lattice. The standard error of mean are shown as the error bars in these figures. The lack of overlap between the error bars confirm the statistical significance of the trend. The observation of small magnitudes of uncertainties at each data point should not be misinterpreted as absolute independence of carrier transport characteristics over spatial distribution of dopant sites. The observation only confirms the independence of the characteristics from spatial distribution as long as the distribution offers uniformity. That carrier transport can be controlled by engineering the spatial distribution of doping concentrations as in homo-junctions of gradient (W/Mo)-doped BVO, will be the subject of a future publication.

III. Results and Discussion

a. Electronic structure in doped BVO:

We used DFT + U to calculate the relative energies of structures when the excess electron associated with the W/Mo atom was localized either at the dopant site, at a nearest neighbor site, at a 2d nearest neighbor site, at a 3d nearest neighbor site, or further away. We used a 3x3x1 super cell, with 36 W (Mo) or V sites available for electron localization including the dopant site. The relative energies are displayed in Figure 2. The calculations reveal a relative stability of charge localization in the nearest neighbor shells compared to the bulk of the lattice. The zero of energy corresponds to the excess electron localized beyond the 4th shell. When the electron is localized at the W site, its relative energy is ~ + 0.660 eV (or ~ 25.5 k_BT with k_BT=0.0259 eV at 300°K), and in the case of Mo, the relative energy for the electron to be at the Mo site is ~ + 0.079 eV (or ~ 3.0 k_BT). Since probabilities of energy states accessible to the electron localization is determined by Boltzmann distribution (Eqs. (4,5), we may conclude that the probability of accessing energy state with electron localized on W site is essentially zero, while that of the electron localizing on Mo site is only ~ 5%.

$$\eta_i = \exp(\frac{-dE_i}{k_B T}) \tag{4}$$

$$dE_i = E_i - E_{bulk} \tag{5}$$

For W, the electron localized on a nearest neighbor site (1^{st} shell) has a relative energy of ~ -0.017 eV (or ~ -0.65 k_BT), it is the most stable shell. For Mo, the most stable shell is the 2^{nd} shell with a relative energy of ~ -0.015 eV (or ~ -0.60 k_BT). The energy profile in Figure 2 is semi-quantitatively similar to the one presented by Wu and Ping.[22] The shape of the energy curve in Figure 2 is suggestive of a region of stability, an interaction region with stabilization energy tailing off to essentially zero beyond the 4^{th} shell. The most stable shell for W-doped BVO is the first nearest neighbor shell while it is the second shell for Mo-doped BVO.

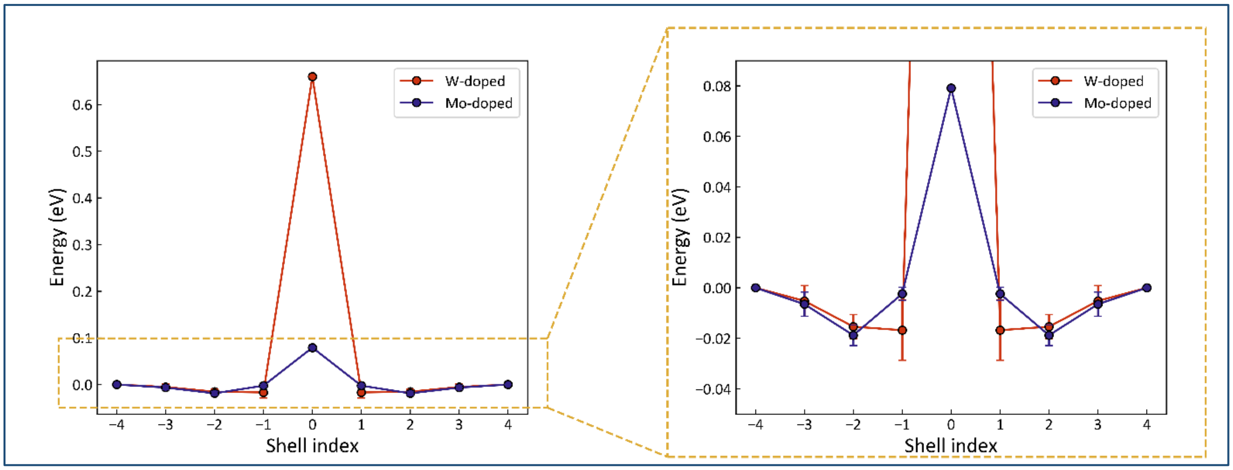

Figure 2. Relative DFT+U energies when the excess electron from W/Mo is localized within vanadium shells away from the dopant site.

Note that the index in Figure 2 is a shell index (0 is the dopant site, 1 is the nearest shell, 2 is the next nearest shell …). The distribution of stabilization energies in the doping region (on sites around the dopant site) cannot be represented in s similar fashion when using other parameters such as site distances, lattice directions, or connectivity between dopant site and electron localization sites. Indeed there exist deviations in the distribution of stabilization energies for sites within shells. Figure 2 arises from averaging the stabilization energies over sites within shells. For simplicity we defined a stabilization energy for each shell through three steps: a/ we calculated the Boltzmann population for each atomic site based on its DFT energy via Eq. (4); b/ we averaged the site populations over the sites within shells; c/ we defined, via Eq. (5), a shell energy (shown in Figure 2) that yields the average population, giving rise to a shell probability via Eq. (6). Here N is the total number of metal sites in the model.

$$dE_{shell\ j} = -k_B T \log(\frac{1}{N}\sum_{i}^{N} \eta_i) \tag{5}$$

$$Shell\ Probability\ (P_j) = \frac{\Omega_j \exp\left(-\frac{dE_{shell\ j}}{k_B T}\right)}{Q} \tag{6}$$

$$Partition\ function, Q = \sum_{j} \Omega_j \exp\left(-\frac{dE_{shell\ j}}{k_B T}\right) \tag{7}$$

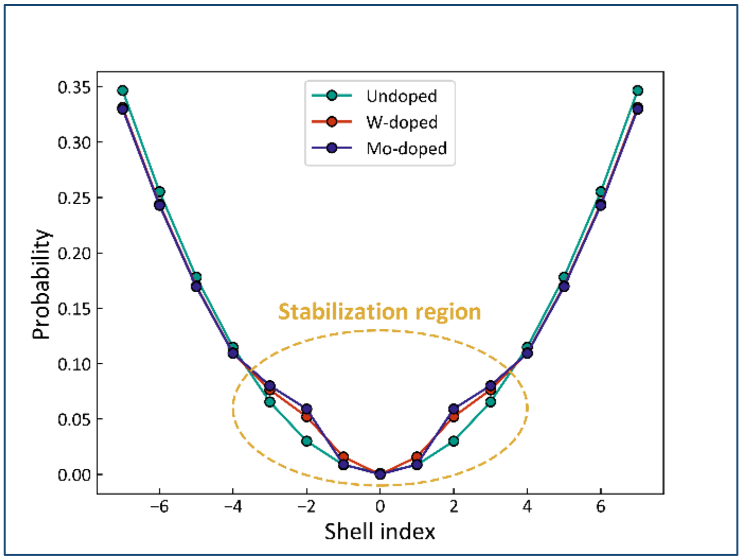

Figure 3. Shell probability distribution around a dopant site in BVO. The increase in probability (highlighted in the yellow oval) for the shells around the dopant site (shell ‘0’) corresponds to the stabilization region.

In this model, all sites within a shell are assumed to be equally accessible (they are equal energy states i.e. degenerate states). Through fitting the data for number of sites within shells (shell j degeneracy Ω_j) up to $j = 4$, shell j degeneracy Ω_j in ms-BVO is reasonably well given by $\Omega_j = 6.429j^2 + 0.486j + 1.057$. The lattice sites may be categorized into three regions based on the shell index j, such as dopant site ($j = 0$), interaction region ($0 < j < 4$), and bulk region ($j \geq 4$). The distribution of shell probabilities as derived from Eq (6). are shown in Figure 3 for un-doped and doped systems within $j_{max} = 7$. While the degeneracy Ω_j is responsible for the large shell probability in the bulk region, it can be seen in Figure 3 that the shell probabilities corresponding to the interaction region are larger for a doped system than for an un-doped system. The larger probabilities indicate an increased accessibility of the electron localization states within the interaction region to the detriment of the dopant site and the ‘bulk’ sites. The nature of the trends shown in Figure 3 remains unaffected with system size (increasing shell index maximum j_{max}), however the difference in the bulk region probabilities between doped and un-doped systems grows more insignificant suggesting a shrinking influence of a single dopant with growing simulation supercell. At the same time, the kinetics in the bulk region are virtually unaffected since all the sites in the bulk are essentially degenerate.

Further discussion about shell probability distribution is included in the Supporting Information. Excess electron localization sites upon Mo or W single doping and co-doping are illustrated in Figure S1 (a) and (b) for selected sites. In all cases, the excess electrons are well localized as confirmed by the spin density plots shown in Figure S2. Upon W/Mo co-doping, there are two excess electrons. The calculated DFT shown in Table S1 indicate that the two electrons prefer to localize on two different V sites. A second configuration has one excess electron localized on a V site and the other electron on the Mo site with a probability of ~ 3 %. Interesting as well is the finding that the two electrons can also form a bi-polaron localized on one single V site, although with a low probability of ~ 1 %.

b. Hopping pathways in doped BVO:

As indicated above, dopant atoms give rise to an interaction region around the doping site whereby the excess electron exhibits a small stabilization compared to the ‘bulk’ region. With Mo doping there is a small probability that the excess electron localize at the Mo site. An excess electron never resides on a W site. In co-doping the stabilization energies are essentially additive.

We investigated the effect of the presence of doping atoms on activation barriers for hops in the neighborhood of dopant atoms. V-to-V hops further away from the dopant atoms than the 4th shell of V atoms do not feel the presence of the dopant atoms and the hopping barriers are unchanged. We selected four V atoms close to the dopant site and we determined the Marcus/Holstein energy profiles for hops involving these atoms. The curves and the energies are presented in Figures S3-S10, and Tables S3 to S10, with some of them involving Mo-to-V hops since Mo atoms have a finite probability to receive an excess electron. These curves complement the exhaustive set of curves reported in our earlier work.[16] The overall outcome is that W and/or Mo doping does not affect the characteristics of hops outside the interaction region created by the dopant atom. Within the interaction region V sites have varying but always small stabilization energies that can very well be accounted for by the quantity ΔG_0 in Marcus/Holstein expression of Eq. (3) or by the Bell/Evans/Polanyi rule[46, 47] on how they affect the activation barriers. In the same vein, changes in energy characteristics for hops involving a Mo atom can be accounted in the same fashion. Considering this small to negligible probability associated with electron transfer processes involving dopant sites, we did not calculate the V_{AB} for these processes. Besides, it is understood that changes in nuclear vibrational modes as a result of thermal fluctuations or crystallographic defects may modify the electron-phonon coupling. [49] However, the nuclear vibrational modes in covalently-bound inorganic semiconductors are largely unaffected particularly at lower doping concentrations [50] under purview in this study (doping concentrations up to 1%). Thus, we continued to use $\Delta G^* \sim 0.37$ eV for electron hops to derive the reorganization energy (λ) from Eq. (3) to be ~1.48 eV.

c. Electron transport in doped BVO:

We defined a model system for W- or Mo-doped BVO, based on the (9x9x4) supercell we used previously for undoped BVO.[16] The number of dopant atoms was 0, 1, 2, 3, and 4 W/Mo atoms within the supercell, corresponding to dopant concentrations up to ~ 0.309 % (in the range of experimental levels). The number of excess electrons in addition to those introduced by the dopant atoms was kept constant at 4 electron polarons (arising from light absorption for example).The KMC data are shown in Figure 4 for electron diffusivity for un-doped, singly-doped (with either W or Mo) and co-doped (doping ratio of W to Mo at 1:1) BVO. For one electron polaron system, the diffusion coefficient (after correction for the difference in activation energy between computation and experiment) is only a factor ~ 5 smaller than the experimental value measured by drift mobility in the presence of an electric field. It can be seen that the average diffusion coefficient exhibits a decrease (cubic dependence) as a function of the electron polaron concentration. Indeed electrons in a multi-electron simulation are not completely free to drift. A move closer to other electrons is less favorable than a move away from other electrons.

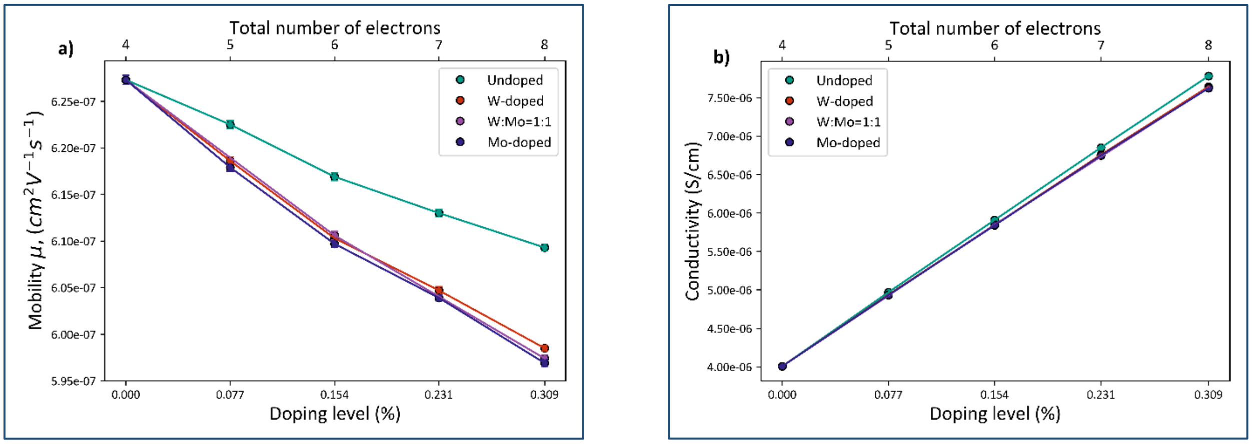

Figure 4. Comparison of electron polaron mobility and conductivity for un-doped and doped BVO systems under the '3Shells' implementation, referring to the number of V shells comprising the small stabilization region around each dopant atom.

When considering 3 nearest neighbor shells as the region of stabilization, every dopant site affects the stability of 97 sites including itself in the simulation supercell size of 9x9x4. Because of this we were able to explore doping levels only up to 0.386 % (5 substitutions among 1296 V sites, here data up to only 4 substitutions shown for easier comparison against co-doped

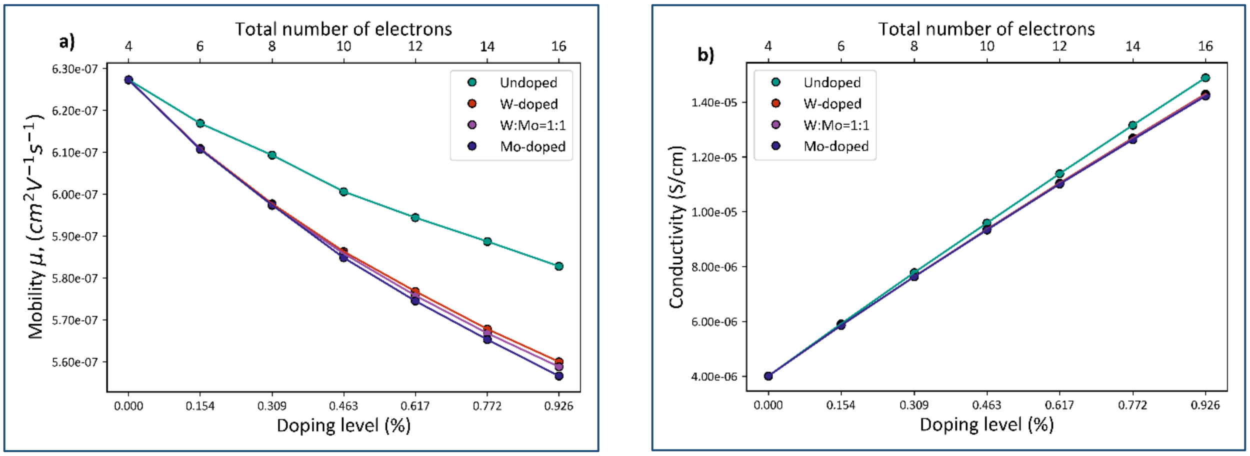

Figure 5. Comparison of electron polaron mobility and conductivity for un-doped and doped BVO systems under the '2Shells' implementation, referring to the number of V shells comprising the small stabilization region around each dopant atom.

simulations) if we assumed non-overlapping stabilization regions. In order to achieve larger doping levels, we repeated the simulations by considering 2 nearest neighbor shells as the region of stabilization, and a total of 37 sites belonging to region of influence (thus the 'bulk' region started from sites belonging to 3rd nearest neighbor shell and beyond). This allowed us to explore doping level up to 1 % (13 substitutions among 1296 V sites). Mobilities and conductivities for the higher doping levels and still four additional excess electrons are shown in Figure 5. Because the stabilization energies are small, we observed only a marginal difference in carrier mobilities between the 2shells- and 3shells- model implementations. The comparative data between the 2shells and 3shells models are presented in Figure S11 in the Supplementary Information.

When comparing the electron mobilities between (singly- and co-doped) doped and un-doped BVO, we observe a marginal decrease (factor of ~ 1.1) in the value of carrier mobility with an increase in doping level. This observation is at odd with the interpretation of a factor of ~ 20 decrease in carrier mobility upon introduction of 1% W doping [51]. However our data supports experiment, in that the intrinsic mobility of electrons in doped BVO is smaller than that of un-doped BVO.

Furthermore, we performed the co-doping simulations with a doping ratio of W to Mo at 1:1. For these simulations, we continued to ensure the non-interaction of any two doping regions to avoid the complexities in the distribution of energetics for electron localization when two or more doping regions overlap. When electron mobilities between singly-doped and co-doped BVO were compared, we noticed that the mean of singly-doped mobilities (W and Mo) and co-doped mobilities are very comparable and within a factor of 0.99-1.01 from each other. However, owing to the shallow nature of the stabilization region, the electron mobilities of W/Mo singly-doped BVO are very close (differ by a maximum factor of only ~1.006 for 12-substitusions). While simulations at higher doping concentrations are necessary for stronger evidence, current observations for co-doping may suggest a linear mixing of the individual contributions from singly-doped systems towards influencing electron transport.

IV. Conclusions

We presented a mesoscale characterization of electron transport in W/Mo-doped BVO. The mesoscale KMC model, informed by first principles-determined electron hopping rates, captures the complex dynamics of electron carriers arising from light absorption and from metal doping. The computations and simulations support the observation that, for the doping level used in experiment, doping atoms do not affect significantly the transport dynamics proper of the charge carriers compared to stoichiometric BVO. W/Mo doping increases the electron carrier concentration, and consequently the conductivity in the electrode. DFT calculations of W/Mo-doped BVO show a shallow interaction region around the doping atom where the excess electron localized on a V atom is much more stable than when localized on the doping atom, and slightly more stable than when the excess electron is localized far away from the doping atom. The calculated V-to-V hopping barriers are little affected within this interaction region and not affected outside this region. Mesoscale KMC simulations indicate that the stabilization regions have little effect on the diffusivity compared to the stoichiometric system because of the smallness of the stabilization. The diffusivity is found to decrease slightly with an increasing number of carriers, but the conductivity of a system with electron polarons arising from doping together with light absorption increases compared to the un-doped system. These findings are consistent with experimental observations. This work will set the foundation to study electron transport in gradient (W/Mo)-doped systems and other mixed phase systems.

Acknowledgements:

V.P and T.L contributed equally to this work. V.P, T.L, C.L, and M.D. designed the study and the calculations and contributed to the interpretation of the data. V.P., T.L. and, M.D. prepared the manuscript. The work was supported in part by the National Natural Science Foundation of China (grant # 21703054). M.D. acknowledges also funds from the University at Buffalo, and support from the U.S. Department of Energy, Office of Science, Office of Basic Energy Sciences, under Award Number(s) DE-SC0019086 (interpretation of the data and writing of the manuscript).

AUTHOR INFORMATION

*Corresponding Author:

Taifeng Liu: tfliu@vip.henu.edu.cn

Michel Dupuis: mdupuis2@buffalo.edu

Notes

The authors declare no competing financial interest.

Associated content

Supporting Information:

The supporting information includes:

1. free energy data of electron polaron localized on the sites involved in the doping region
2. corresponding spin density contours
3. Interpolation energy curves for electron hop between sites involved in doping region.
4. Comparison of electron mobility curves between 2-shell, 3-shell models
5. Bar plot showing shell-wise residence frequency

V. Appendix:

a. Program Description:

We developed a cross-platform object-oriented library of python modules and scripts called PyCT (**Py**thon-based **C**harge **T**ransport) to perform lattice-based KMC simulations of charge carrier kinetics in crystalline semiconductor materials at mesoscopic length and time scales. The library is hosted as a private repository on GitHub. Interested users can contact one of us (VP) to get access at the repository. The workflow of the KMC code is depicted in Figure A1. The code consists of two essential components, a 'Simulation System' and a 'Simulation Engine'.

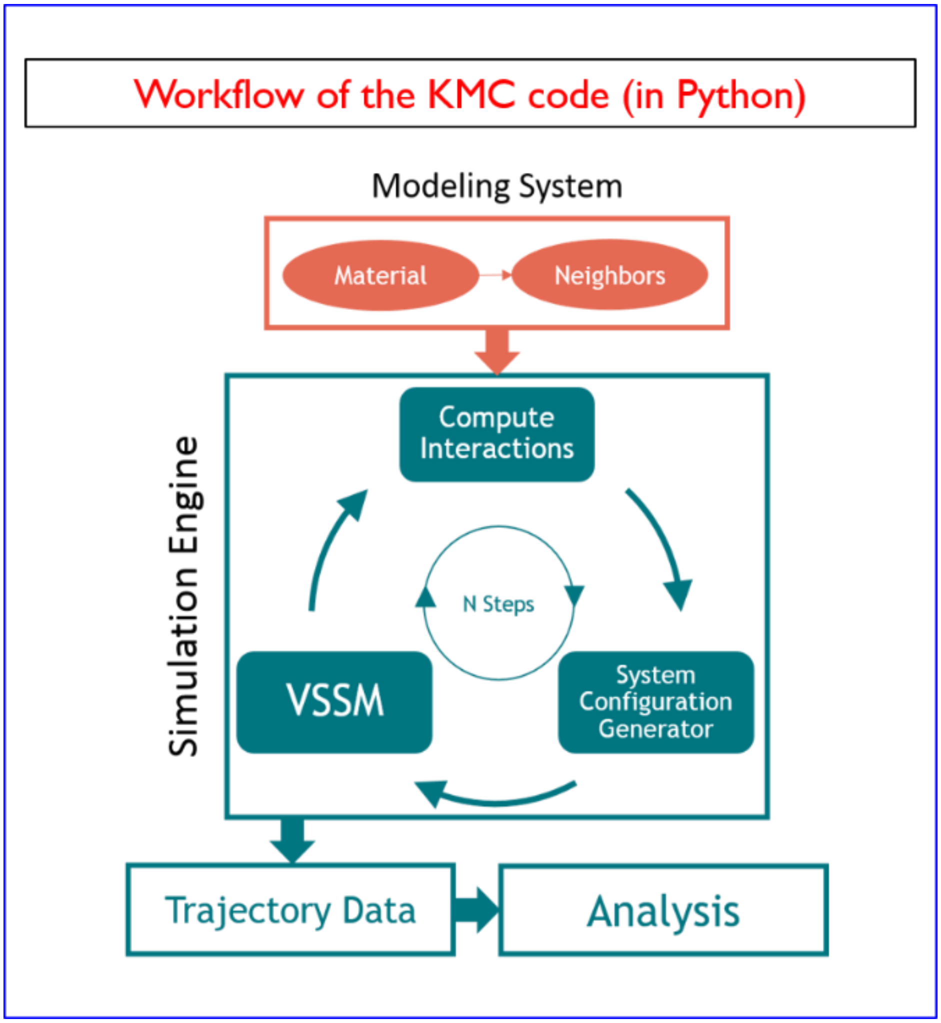

Figure A1. Workflow of the Python KMC code - PyCT -.

The 'Simulation System' includes two object definitions: the first called 'Material' with all physical parameters related to the material of interest, including system size, atomic coordinates, charge hopping parameters (reorganization energy λ and electronic coupling V_{AB} from

Marcus/Holstein theory of hopping model. [52]) The second object is 'Neighbors' that contains functions to generate the cell lists for hopping neighbors and atom pairs interacting within the short-range part of Ewald summation.

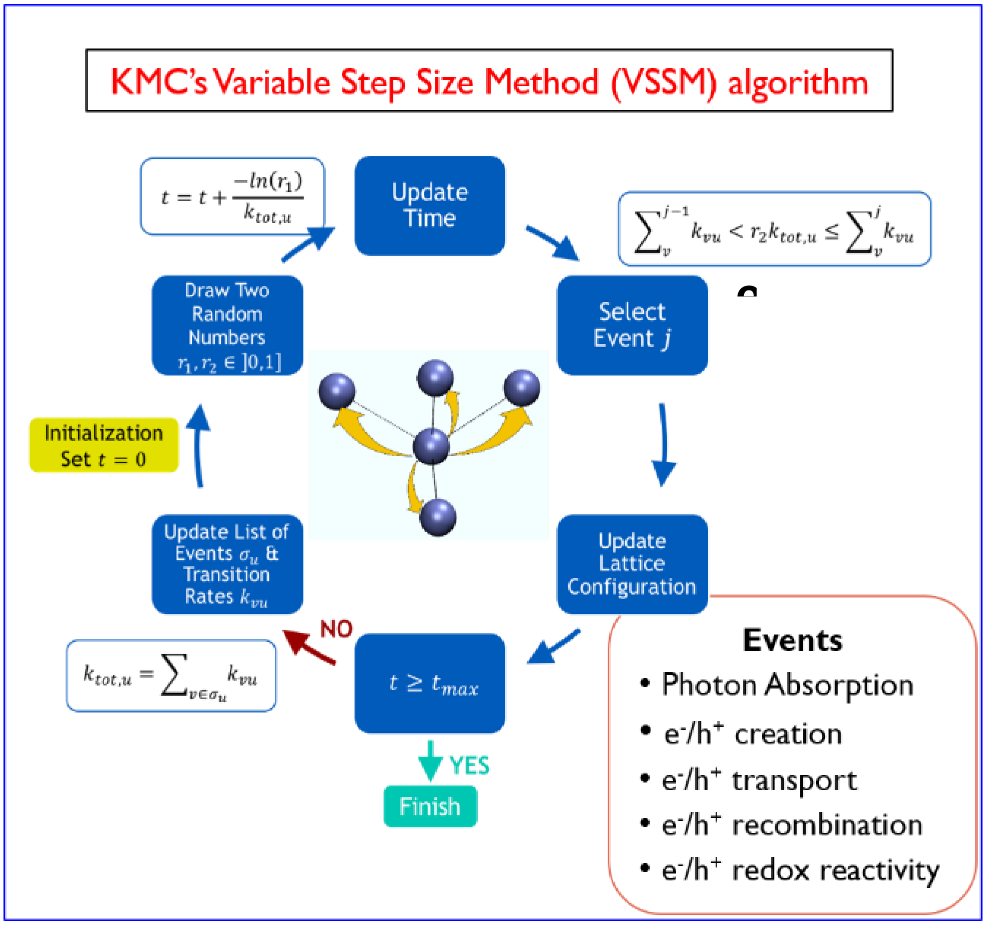

Figure A2. Schematics of the Variable Step Size Method (VSSM) algorithm for KMC simulations.

The second essential component of the code, the 'Simulation Engine', includes a collection of objects related to the Variable Step Size Method (VSSM) implementation of KMC depicted in Figure A2. The charge transfer reactions are modelled between neighboring sites via small polaron hopping steps. [36] The charge transfer parameters for the elementary processes originate preferably from first-principle calculations or from experiment. The long-range Coulombic interactions between polaron-polaron, polaron-lattice are computed by Ewald summation technique. Since the KMC simulations are performed over a static lattice, we derived for computational efficiency an expression to compute directly the key quantity of interest, the change in free energy (ΔG_0). This strategy reduces the computational scaling from $O(N^2)$ to $O(N)$, where N is the total number of ions in the system. Instantaneous kinetic rates are computed using the activation energies as estimated from change in (ΔG_0) using Brønsted-Evans-Polanyi relation [53] or Marcus/Holstein expression. Since the spatial distribution of charges changes at each time step, the quantities (ΔG_0) and the associated process rates k must be computed for all possible processes at each instant of time.

From Eq. (3) above, the quantity ΔG_0, the instantaneous energy 'defect' for a given hop, consists of two components: (1) one arising from the total electrostatic energy of the instantaneous charge distribution and calculated by the Ewald formalism, and (2) shift applied from the electron localization energetics due to doping atoms:

$$\Delta G_0 = \Delta G_{0,Ewald} + \Delta G_{0,Shift} \qquad \text{(A1)}$$

For a charge transferring from site $\boldsymbol{k}$ to site $\boldsymbol{k'}$, the change in the system energy is given by:

$$\Delta G_{0,Ewald} = q_c \left[2 \sum_i q_i^{old} (P_{ik'} - P_{ik}) + q_c (P_{kk} + P_{k'k'} - 2P_{kk'}) \right] \qquad \text{(A2)}$$

where

$$P_{ij} = \left[\sum_n \frac{erfc\left(\sqrt{\alpha}\left|\overline{r_{ij}} + \overline{n}\right|\right)}{2\left|\overline{r_{ij}} + \overline{n}\right|} + \sum_{k\neq 0} \frac{2\pi}{V} \frac{e^{-k^2/4\alpha} \cos k . r_{ij}}{k^2} \right] \qquad \text{(A3)}$$

In doped-BVO systems, an interaction energy is given to electrons within the interaction region of a dopant atom. If we denote $\delta E(q_i)$ the instantaneous energy stabilization contribution arising from the carriers within the interaction region of any dopant, upon a change of charge configuration associated with a KMC move (an electron may move into an interaction region or move out of an interaction region), the configuration stabilization energy $\Delta G_{0,Shift}$ is given by:

$$\Delta G_{0,Shift} = \delta E(q_i^{new}) - \delta E(q_i^{old}) \qquad \text{(A4)}$$

The quantity ΔG_0 is computed within the function 'get_process_rates' that returns the kinetic rate of the process under consideration via the two equations:

$$\Delta G^* = \frac{(\lambda + \Delta G^0)^2}{4\lambda} - V_{AB} \qquad \text{(A5)}$$

$$k_{et} = n\nu_n \exp\left(-\frac{\Delta G^*}{k_B T}\right) \tag{A6}$$

The choice of process to be enacted is made by generating a random number x_1 within the function ‘do_kmc_steps’ as defined below:

$$\sum_{j=1}^{i-1} \frac{k_{et}^j}{\Gamma} < x_1 \leq \sum_{j=1}^{i} \frac{k_{et}^j}{\Gamma} \tag{A7}$$

$$\Gamma = \sum_{j=1}^{n} k_{et}^j \tag{A8}$$

The code is outlined in Figure A3.

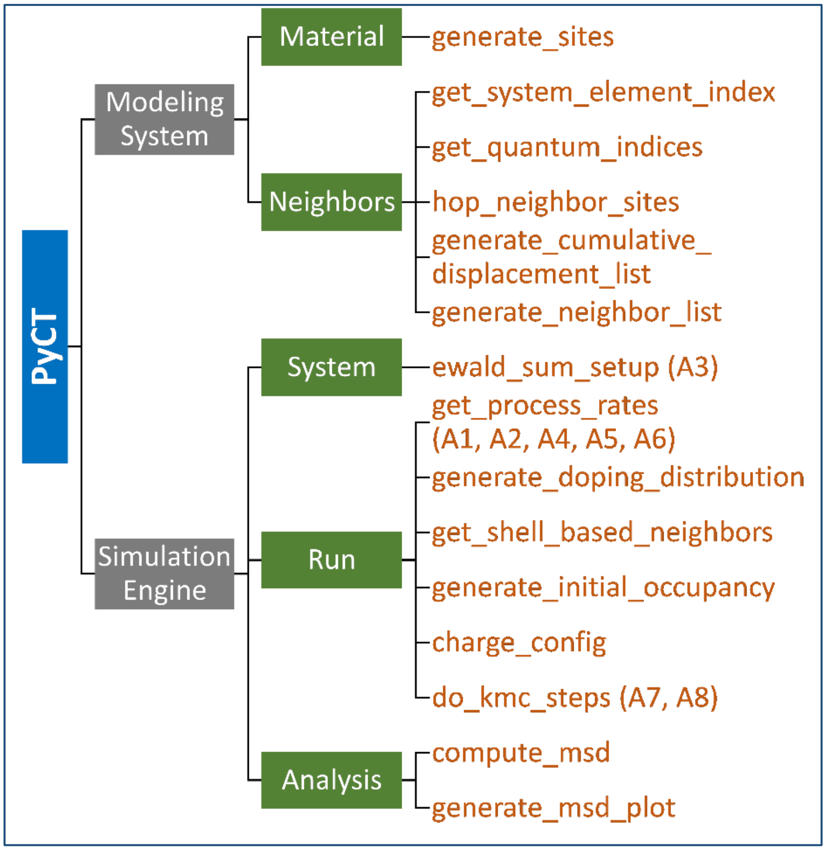

Figure A3 – PyCT - KMC code outline; Eqs. (A1 to A8) are shown next to the functions where they are implemented.

b. Further discussion on probability distribution

The nature of internal distribution of probabilities within the lattice may be quantified by segmenting between the pre-defined regions as presented in Table A1. The net increase in the probability for doping region (dopant site + interaction region) upon doping is compensated through a decrease in the probability for bulk region.

Table A1. Region-specific probabilities in un-doped and W/Mo-doped systems for $j_{max} = 7$

	Dopant site	Interaction region	Bulk region
Undoped	0.001	0.104	0.895
W-doped	0.000 (-0.001)	0.145 (+0.041)	0.855 (-0.040)
Mo-doped	0.001 (-0.000)	0.148 (+0.044)	0.851 (-0.044)

$$\frac{P_{doped}}{P_{undoped}} = \frac{N \exp\left(-\frac{dE_{shell\ j,\ doped}}{k_B T}\right)}{Q_{doped}} \tag{A9}$$

The change in shell accessibility upon doping may also be noticed through the ratio of doped to un-doped probabilities ($P_{doped}/P_{undoped}$) as defined in Eq. (A9) with the quantity plotted against shell index j in Fig. A4a. The zero or near-zero values of the ratio at the dopant site (shell 0) arise from the positive relative energy for electron localization at the dopant site, as discussed in the main text. In the interaction region the ratio is larger than 1.0, indicating increased stability for electron localization upon doping. The ratio peaks at $j = 1$ for W-doped and $j = 2$ for Mo-doped systems, consistent with the energetic distribution shown in the inset of Figure 2. Owing to zero stabilization energies of the 'bulk' region, the ratio remains constant at 0.828 for W-doped and 0.813 for Mo-doped systems. The decrease in ratio for the bulk region from unity is a consequence of the probability distributions within the lattice as shown in Table A1. The constant value across the bulk shells suggest that the charge transport kinetics in this region are unaffected by the dopant site and continue to resemble that of an un-doped system.

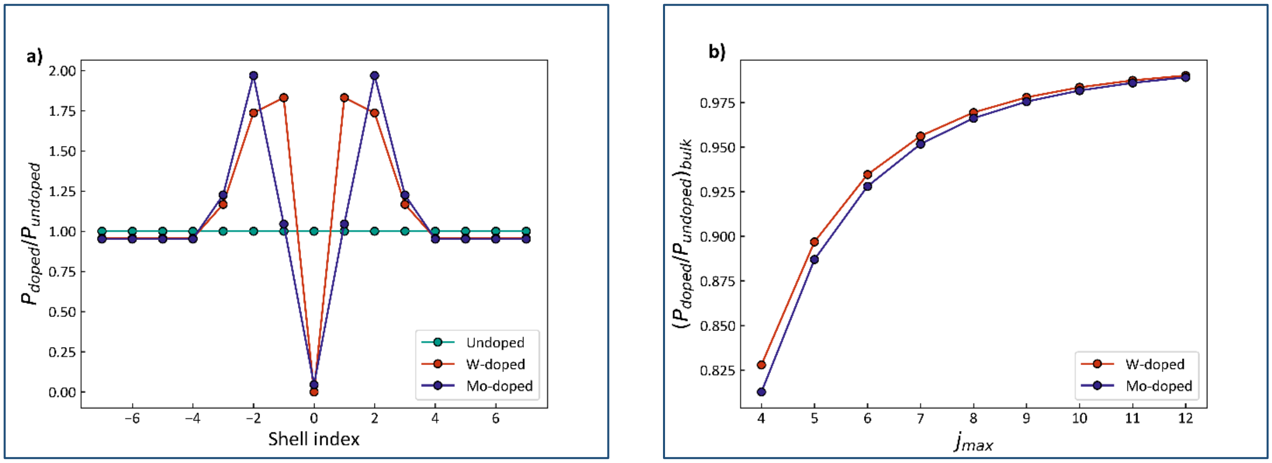

Figure A4. (a) Ratio of doped to un-doped probabilities plotted against shell index j, (b) bulk value of probability ratio plotted against j_{max}

The probability ratio for bulk region, as shown in Fig. A4b shows an asymptotic behavior with increasing maximum shell index (j_{max}). Such quick convergence towards unity further reinforces the finiteness of the impact of the W/Mo-doping over the neighboring bulk in ms-BVO lattice.

A glossary of the variables used in the equations above includes:

- q_c: charge of the carrier (-1 for electron)
- q_i^{old}: Charge configuration in the old state where charge located at site k.
- q_i^{new}: Charge configuration in the old state where charge located at site k'.
- α: Ewald summation parameter. Used $\alpha = 0.18$ for computational efficiency.
- $\overline{r_{ij}}$: vector connecting ion i to ion j
- V: system volume
- $\bar{n}$: lattice vector in real space
- $\boldsymbol{k}$: lattice vector in Fourier space
- $\delta E(q_i)$: Energy shift to be applied corresponding to the charge configuration q_i

References:

1. Sivula, K. and R. van de Krol, *Semiconducting materials for photoelectrochemical energy conversion.* Nature Reviews Materials, 2016. **1**: p. 15010.
2. Walter, M.G., et al., *Solar Water Splitting Cells.* Chemical Reviews, 2010. **110**(11): p. 6446-6473.
3. Fatwa, F.A. and P.B. Sean, *Recent developments in complex metal oxide photoelectrodes.* Journal of Physics D: Applied Physics, 2017. **50**(19): p. 193002.
4. Woodhouse, M. and B.A. Parkinson, *Combinatorial approaches for the identification and optimization of oxide semiconductors for efficient solar photoelectrolysis.* Chemical Society Reviews, 2009. **38**(1): p. 197-210.
5. Liang, Y., et al., *Highly Improved Quantum Efficiencies for Thin Film BiVO4 Photoanodes.* The Journal of Physical Chemistry C, 2011. **115**(35): p. 17594-17598.
6. Cooper, J.K., et al., *Indirect Bandgap and Optical Properties of Monoclinic Bismuth Vanadate.* The Journal of Physical Chemistry C, 2015. **119**(6): p. 2969-2974.
7. Kim, T.W. and K.-S. Choi, *Nanoporous* $BiVO_4$ *Photoanodes with Dual-Layer Oxygen Evolution Catalysts for Solar Water Splitting.* Science, 2014. **343**(6174): p. 990-994.
8. Park, H.S., et al., *Factors in the Metal Doping of BiVO4 for Improved Photoelectrocatalytic Activity as Studied by Scanning Electrochemical Microscopy and First-Principles Density-Functional Calculation.* The Journal of Physical Chemistry C, 2011. **115**(36): p. 17870-17879.
9. Park, Y., K.J. McDonald, and K.-S. Choi, *Progress in bismuth vanadate photoanodes for use in solar water oxidation.* Chemical Society Reviews, 2013. **42**(6): p. 2321-2337.
10. Le, C., et al., *Mo-Doped BiVO4 Photoanodes Synthesized by Reactive Sputtering.* ChemSusChem, 2015. **8**(6): p. 1066-1071.
11. Yao, W., H. Iwai, and J. Ye, *Effects of molybdenum substitution on the photocatalytic behavior of BiVO4.* Dalton Transactions, 2008(11): p. 1426-1430.
12. Ye, H., et al., *Rapid Screening of BiVO4-Based Photocatalysts by Scanning Electrochemical Microscopy (SECM) and Studies of Their Photoelectrochemical Properties.* The Journal of Physical Chemistry C, 2010. **114**(31): p. 13322-13328.
13. Li, M., L. Zhao, and L. Guo, *Preparation and photoelectrochemical study of BiVO4 thin films deposited by ultrasonic spray pyrolysis.* International Journal of Hydrogen Energy, 2010. **35**(13): p. 7127-7133.
14. Yin, W.-J., et al., *Doping properties of monoclinic* $BiVO_4$ *studied by first-principles density-functional theory.* Physical Review B, 2011. **83**(15): p. 155102.
15. Zhong, D.K., S. Choi, and D.R. Gamelin, *Near-Complete Suppression of Surface Recombination in Solar Photoelectrolysis by "Co-Pi" Catalyst-Modified W:BiVO4.* Journal of the American Chemical Society, 2011. **133**(45): p. 18370-18377.
16. Liu, T., et al., *Bimodal hole transport in bulk BiVO4 from computation.* Journal of Materials Chemistry, 2018. **6**: p. 3714-3723.
17. Liu, T., et al., *The nature of photogenerated charge separation among different crystal facets of BiVO4 studied by density functional theory.* Physical Chemistry Chemical Physics, 2015. **17**(36): p. 23503-23510.
18. Jovic, V., et al., *Soft X-ray spectroscopic studies of the electronic structure of M:BiVO4 (M = Mo, W) single crystals.* Journal of Materials Chemistry A, 2015. **3**(47): p. 23743-23753.

19. Jovic, V., et al., *A soft X-ray spectroscopic perspective of electron localization and transport in tungsten doped bismuth vanadate single crystals.* Physical Chemistry Chemical Physics, 2016. **18**(46): p. 31958-31965.
20. Abdi, F.F., et al., *Efficient solar water splitting by enhanced charge separation in a bismuth vanadate-silicon tandem photoelectrode.* Nature Communications, 2013. **4**: p. 2195-2201.
21. Han, L.H., et al., *Efficient Water-Splitting Device Based on a Bismuth Vanadate Photoanode and Thin-Film Silicon Solar Cells.* Chemsuschem, 2014. **7**(10): p. 2832-2838.
22. Wu, F. and Y. Ping, *Combining Landau Zener theory and kinetic Monte Carlo sampling for small polaron mobility of doped BiVO4.* Condensed-Mat.mtrl-sci, 2018. **arXiv:1808.02507**
23. Zhang, W., et al., *Unconventional relation between charge transport and photocurrent via boosting small polaron hopping for photoelectrochemical water splitting.* Acs Energy Letters, 2018. **3**: p. 2232-2239.
24. Rettie, A.J.E., et al., *Anisotropic small-polaron hopping in W:BiVO4 single crystals.* Applied Physics Letters, 2015. **106**(2): p. 022106-022110.
25. Yin, W.-J., et al., *Doping properties of monoclinic BiVO 4 studied by first-principles density-functional theory*. Physical Review B, 2011. **83**(15): p. 155102.
26. Ding, K., et al., *Why the photocatalytic activity of Mo-doped BiVO 4 is enhanced: a comprehensive density functional study*. Physical Chemistry Chemical Physics, 2014. **16**(26): p. 13465-13476.
27. Rettie, A.J.E., et al., *Unravelling Small-Polaron Transport in Metal Oxide Photoelectrodes.* The Journal of Physical Chemistry Letters, 2016. **7**(3): p. 471-479.
28. Kresse, G. and J. Furthmuller, *Efficient iterative schemes for ab initio total-energy calculations using a plane-wave basis set.* Physical Review B, 1996. **54**(16): p. 11169-11186.
29. Kresse, G. and J. Furthmuller, *Efficiency of ab-initio total energy calculations for metals and semiconductors using a plane-wave basis set.* Computational Materials Science, 1996. **6**(1): p. 15-50.
30. Perdew, J.P., K. Burke, and M. Ernzerhof, *Generalized gradient approximation made simple (vol 77, pg 3865, 1996).* Physical Review Letters, 1997. **78**(7): p. 1396-1396.
31. Blochl, P.E., *Projector augmented-wave method.* Physical Review B, 1994. **50**(24): p. 17953-17979.
32. Kresse, G. and D. Joubert, *From ultrasoft pseudopotentials to the projector augmented-wave method.* Physical Review B, 1999. **59**(3): p. 1758-1775.
33. Dudarev, S.L., et al., *Electron-energy-loss spectra and the structural stability of nickel oxide: An LSDA+U study.* Physical Review B, 1998. **57**(3): p. 1505-1509.
34. Monkhorst, H.J. and J.D. Pack, *Special points for brillouin-zone integrations.* Physical Review B, 1976. **13**(12): p. 5188-5192.
35. Rosso, K.M. and M. Dupuis, *Electron transfer in environmental systems: a frontier for theoretical chemistry.* Theoretical Chemistry Accounts, 2006. **116**(1-3): p. 124-136.
36. Rosso, K.M., D.M.A. Smith, and M. Dupuis, *An ab initio model of electron transport in hematite (α-Fe2O3) basal planes.* The Journal of Chemical Physics, 2003. **118**(14): p. 6455-6466.

37. Deskins, N.A. and M. Dupuis, *Electron transport via polaron hopping in bulk TiO2: A density functional theory characterization.* Physical Review B, 2007. **75**: p. 195212-195221.
38. Deskins, N.A. and M. Dupuis, *Intrinsic Hole Migration Rates in TiO2 from Density Functional Theory.* Journal of Physical Chemistry C, 2009. **113**: p. 346-358.
39. Emin, D. and T. Holstein, *Adiabatic Theory of Hall Mobility of Small Polaron in Hopping Regime.* Bulletin of the American Physical Society, 1968. **13**(3): p. 464.
40. Emin, D. and T. Holstein, *Studies of Small Polaron Motion. 4. Adiabatic Theory of Hall Effects.* Annals of Physics, 1969. **53**(3): p. 439-520.
41. Liu, T., M. Dupuis, and C. Li, *Band Structure Engineering: Insights from Defects, Band Gap, and Electron Mobility, from Study of Magnesium Tantalate.* Journal of Physical Chemistry C, 2016. **120**(13): p. 6930-6937.
42. Wang, L.J., et al., *Multiscale study of charge mobility of organic semiconductor with dynamic disorders.* Physical Chemistry Chemical Physics, 2010. **12**(13): p. 3309-3314.
43. Hoffmann, M.J., S. Matera, and K. Reuter, *kmos: A lattice kinetic Monte Carlo framework.* Computer Physics Communications, 2014. **185**(7): p. 2138-2150.
44. Leetmaa, M. and N.V. Skorodumova, *KMCLib: A general framework for lattice kinetic Monte Carlo (KMC) simulations.* Computer Physics Communications, 2014. **185**(9): p. 2340-2349.
45. Yu, J., et al., *Kinetic Monte Carlo Study of Ambipolar Lithium Ion and Electron-Polaron Diffusion into Nanostructured TiO2.* Journal of Physical Chemistry Letters, 2012. **3**(15): p. 2076-2081.
46. Bell, R.P., *The theory of reactions involving proton transfers.* Proceedings of the Royal Society of London, Serie A, 1936. **154**: p. 414.
47. Evans, M.G. and M. Polanyi, Journal of the Chemical Society, Faraday Transactions, 1936. **32**: p. 1340.
48. Ju, M.G., et al., *Origin of high photocatalytic properties in the mixed-phase TiO2: a first-principles theoretical study.* ACS Appl Mater Interfaces, 2014. **6**(15): p. 12885-92.
49. Wang, L., et al., *Multiscale study of charge mobility of organic semiconductor with dynamic disorders.* Physical Chemistry Chemical Physics, 2010. **12**(13): p. 3309-3314.
50. Merupo, V.-I., et al., *Structural and optical characterization of ball-milled copper-doped bismuth vanadium oxide (BiVO4).* CrystEngComm, 2015. **17**(17): p. 3366-3375.
51. Abdi, F.F., et al., *The Origin of Slow Carrier Transport in BiVO4 Thin Film Photoanodes: A Time-Resolved Microwave Conductivity Study.* The Journal of Physical Chemistry Letters, 2013. **4**(16): p. 2752-2757.
52. Marcus, R.A. and N. Sutin, *Electron transfers in chemistry and biology.* Biochimica et Biophysica Acta (BBA) - Reviews on Bioenergetics, 1985. **811**(3): p. 265-322.
53. Hauser, A.W., et al., *A systematic study on Pt based, subnanometer-sized alloy cluster catalysts for alkane dehydrogenation: effects of intermetallic interaction.* Physical Chemistry Chemical Physics, 2016. **18**(16): p. 10906-10917.

TOC Graphics:

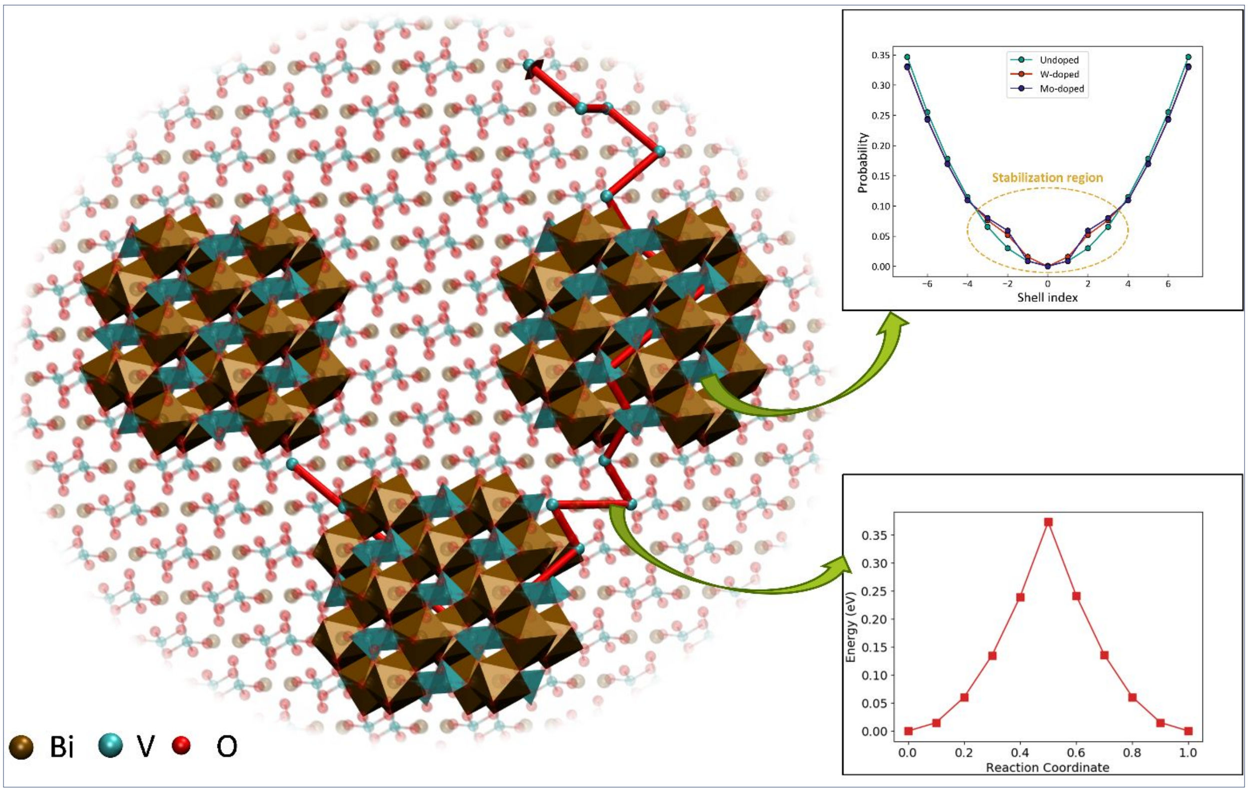

TOC Caption: A first principles-based mesoscale characterization of electron transport in W/Mo-doped $BiVO_4$ reveals the existence of “stabilization” regions around dopant sites. The stabilization regions decrease slightly the electron polaron mobility, albeit the overall electrode conductivity increases.